# Observation of Fresnel diffraction in a two-beam laser interferometer

A. Bergamin, G. Cavagnero, and G. Mana
*Consiglio Nazionale delle Richerche, Istituto di Metrologia "G. Colonnetti," strada delle Cacce 73, 10135 Torino, Italy*
(Received 21 July 1993)

A displacement-angle interferometer capable of $10^{-6}$ resolution in fringe division was developed for the precise measurement of the silicon (220) lattice spacing by x-ray and optical interferometry. With a view to achieving $10^{-8}$ measurement uncertainty, the interference pattern was studied by the Fresnel (Gaussian) scalar approximation of the free-space propagation of interfering beams. Imperfect alignment and diffraction phenomena having been identified, and subsequently experimentally proved, as important error sources, remedial steps were identified and taken with consequent improvement of the experiment accuracy. The investigation brought into light theoretical and experimental evidences of corrections to the interference phase which were overlooked in previous analyses.

PACS number(s): 42.62.Eh, 06.30.Bp, 07.60.Ly, 06.20.Jr

## I. INTRODUCTION

The stabilized laser sources now readily available have made it possible in the high-resolution interferometric measurements of spatial dimensions to state accuracies greatly exceeding the capabilities of previous techniques and to observe interference features previously unresolved.

According to the principles of interferometry, a laser beam is split into two beams, the reference and measuring, which will recombine after propagating in the interferometer arms. If a plane wave is assumed to propagate into the interferometer, a simple ray tracing shows (Fig. 1) that by moving a mirror over the distance $s$, the interfering beams shift longitudinally with respect to each other by $2s\cos\beta$, with $\beta$ denoting the deviation from perfect alignment. The difficulty of high-precision interferometric measurements is related, among other phenomena, especially to imperfect alignment and diffraction: a real interferometer necessarily limits transverse extension of the plane wave which is assumed to illuminate it, so that diffraction is always present. As a result, the wave fronts bend and their spacing varies from one point to another and is different from the wavelength of a plane wave. In precision measurements, diffraction, which increases quadratically with beam clip, is a basic problem that was extensively investigated both theoretically [1–3] and experimentally [4].

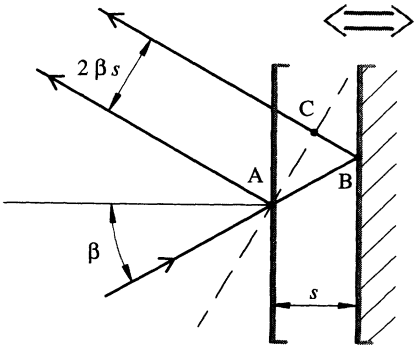


FIG. 1. Ray tracing of measuring beam reflection. The broken line represents a reflected wave front. From elementary geometry, longitudinal and transverse shearings are related to mirror displacement by $\overline{AB} + \overline{BC} = 2s(1 - \beta^2/2)$ and $\overline{AC} = 2\beta s$.

The authors of the present article are working on applications of x-ray and optical interferometry in the measurement of the silicon $d_{220}$ lattice spacing [5]. The precision measurement of $d_{220}$ is an essential step for the determination of the Avogadro constant, for the measurement of the de Broglie wavelength of thermal neutrons, for the extension of the electromagnetic wavelength scale to the x-ray and $\gamma$-ray regions, and for the absolute determination of atomic masses. The $d_{220}$ experiment is a basic exercise of dimensional metrology because displacement and tilts of a silicon crystal, which constitutes the movable part of the x-ray and optical interferometer, must be measured with at least 1 pm accuracy and 1 nrad resolution, respectively. With this in view, the authors developed a Michelson-type interferometer capable of measuring position and attitude simultaneously and whose resolution is limited only by photon counting noise [6]. Quality of the interference is essential to the experiment and, in view of the $10^{-8}$ desired accuracy, the authors have been stimulated to carry out an experimental and theoretical analysis of possible errors in interferometer operation.

The interference of two Gaussian beams was discussed by one of the authors [7], and the analysis of diffraction was extended to the general case of noncollinear beams. As Fig. 1 shows, if the laser beam is imperfectly aligned, when the mirror is moved the interfering beams shear laterally by $2s\sin\beta \approx 2\beta s$. In the running of the experiment it appeared clear that, owing to an incomplete physical interpretation, the contribution by transverse shearing to the interference was overlooked in the previous analysis: whereas shearing has no influence in the case of an unlimited plane wave, it is not so if the wave fronts are bent by diffraction. The necessity of coping also with this phenomenon prompted the investigation of the combined effects of diffraction and imperfect alignment.

The article first considers a geometry parametrization

 

by which the effect of transverse shearing in the interference of two Gaussian beams is described in the simplest way. Then it shows that angular and transverse shearings produce the same interference pattern and that, when this pattern is analyzed, a seeming wave front rotation is detected. A simple relation, which can be verified experimentally, is found between measured quantities and wavefront bending by diffraction. The article proves that mathematical investigation accounts for the observed anomaly of interference and that the combined effect of diffraction and imperfect alignment can be theoretically described and experimentally examined making it possible dimensional measurements with $10^{-6}$ of a period accuracy in fringe division.

## II. EXPERIMENTAL SETUP

The x-ray and optical interferometer is schematically shown in Fig. 2. The x-ray interferometer is geometrically similar to a Mach-Zehnder interferometer [8]. The incoming x-ray beam is coherently split and recombined by multiple Laue diffraction to obtain interfering beams both propagating in the same direction. The interference pattern is scanned either by varying the length of the path in one arm of the interferometer (as is done in the optical equivalents) or by moving any one of the three crystals (the analyzing crystal in the present case) orthogonally to the diffracting planes. In the latter case, as predicted by the dynamical theory of x-ray scattering in perfect crystals, the interference period, actually 0.192 nm, is equal to that of the diffracting planes. Owing to its extreme sensitivity and linearity, the x-ray interferometer performs movement and rotation measurements which are accurate to picometer and nanoradian levels [9–11]. Analyzer yawing is revealed by the fine structure of the phase shift between the fringes belonging to the transmitted and diffracted beams [12], and analyzer pitching by the phase shift between fringes belonging to the top and bottom portions of the interference pattern

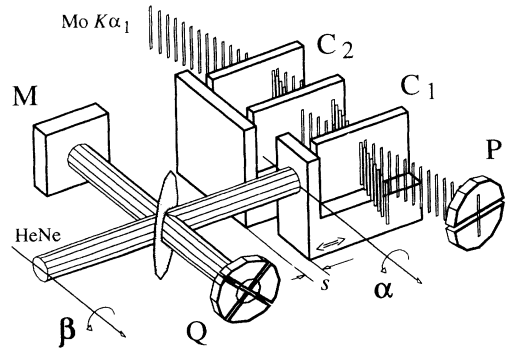


FIG. 2. Schematic drawing of the x-ray and optical interferometer. Mo $K\alpha_1$ x-ray beam, C1 and C2 fixed and movable (analyzer) crystals of the x-ray interferometer, P and Q position-sensitive detectors, He-Ne laser beam, M fixed mirror. X-ray and optical fringes are scanned by moving the analyzer over the distance $s$. Laser beam and interferometer alignments are varied by tilting the beam-delivering fiber (rotation $\beta$) and the analyzer (rotation $\alpha$).

[9]. Phase shifts are estimated by the fit of the relevant photon counts versus analyzer displacement [10]. The standard deviation of estimates is $10^{-3}$ of a fringe period, which, in the case of the pitch measurement, is equivalent to 1 nrad error.

Though the interference pattern is very sensitive to the analyzer attitude, measurements of pitch and yaw by x-ray interferometry are not suitable for on-line correction of guiding errors by servo-control because of the limited bandwidth of the measuring chain. Attitude measurements by optical interferometry were therefore investigated. The final technique [13] is based on an extension of angle interferometry in which the interferometer arms are folded so as to use a single beam. Different parts of the beam strike different parts of the analyzer and, as in standard angle interferometry, the difference in the optical paths, $\Delta s = \alpha D$, is proportional to the analyzer rotation $\alpha$ with $D$ the distance between the centers of the two spots. The interference pattern being integrated on the four slices of a four-quadrant diode, the angle values are given by the differential displacements between the vertical and the horizontal portions of the spot. The displacement is simultaneously obtained by averaging the four partial signals.

When operating in vacuo, the necessary resolution is obtained by polarization encoding [14] and phase modulation [6]. With this technique, the phase shift between the two linearly and orthogonally polarized beam components, which represent the reference and the measuring beams, is modulated by a Pockels's cell and noise is corrected for by driving the modulator to lock to zero the static phase shift at the interferometer entrance. At each dark or bright fringe (the balance position of the interferometer) a $10^{-6}$ resolution in fringe division has been demonstrated, which is equivalent to sensitivity of 1 pm and 1 nrad in displacement and angle measurements, respectively. Positioning with picometer resolution and the attenuation of seismic disturbances are made possible by a feedback loop driving a piezoelectric element to lock the guide to a reference value or to a reference path [15].

## III. THEORY

With reference to the Fig. 3, let us consider two interfering beams produced by an interferometer illuminated by a monochromatic Gaussian beam having unit amplitude, spot size $w_0$ at the beam waist, wave number $k = 2\pi/\lambda$, and confocal parameter $b = kw_0^2$. Let us also denote by $\boldsymbol{r}$ the radial distance from the beam axis, by $2\alpha$ and $2s\cos\beta$ the misalignment and the shift between the interfering wavefronts ($\alpha$ and $s$ being the geometric misalignment and shift between the interferometer mirrors), by $z$ the distance of the observation plane from the beam waist, and by $w$ and $1/R$ the spot size and wavefront curvature at the observation plane [16]. A reference frame is attached to each beam. Each of the frames has its origin at the beam waist and its $\zeta$ axis coincides with the beam axis, the positive direction being toward the observation plane. The transformation law between the two frames is given by

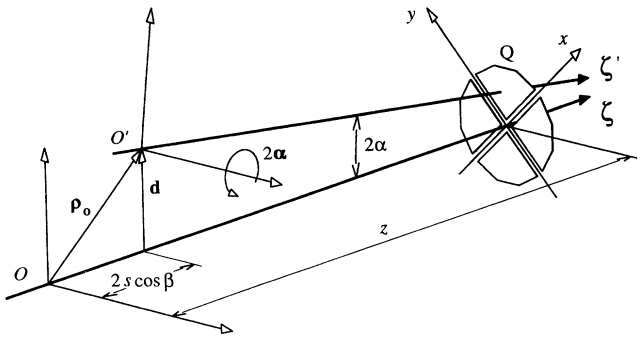


FIG. 3. Schematic drawing of the interference of noncollinear Gaussian beams. The virtual images of the beam waists are denoted by $O$ and $O'$, beam axes are $\zeta$ and $\zeta'$. The integration regions in the observation plane are defined by borders $x$ and $y$ of the position-sensitive detector Q.

$$\boldsymbol{\varrho}' = (\boldsymbol{\varrho} - \boldsymbol{\varrho}_0) + 2\boldsymbol{\alpha} \times (\boldsymbol{\varrho} - \boldsymbol{\varrho}_0), \tag{1}$$

in which cylindrical coordinates have been used, $\boldsymbol{\varrho}_0 = d\hat{\boldsymbol{r}}_0 + 2s\cos\beta\hat{\boldsymbol{\zeta}}$, the hat denotes the unit vectors, and $\cos\beta$ describes the projection of $2s$ (the displacement orthogonal to the mirror surface) on the interferometer baseline (the direction of the measuring beam). The transverse shearing of the interfering beams is given by

$$\boldsymbol{d} = d\hat{\boldsymbol{r}}_0 = 2s\boldsymbol{\beta} \times \hat{\boldsymbol{\zeta}} - 2z_I\boldsymbol{\alpha} \times \hat{\boldsymbol{\zeta}}, \tag{2}$$

where $z_I$ is the distance of the interferometer mirrors from the beam waist when $s = 0$. Rotations around arbitrary axes are described by the vectors $\boldsymbol{\alpha}$ and $\boldsymbol{\beta}$. Since we are interested in small deviations from ideal geometry, $s = \alpha = \beta = 0$, and since the Fresnel approximation [17] is already implicit in the law of Gaussian-beam propagation, we consider only the lowest order contributions of the interferometer geometry and the quadratic contributions of the transverse coordinates to the phase of the interference pattern. Thus, in the region of Fresnel diffraction, the intensity distribution is

$$I(\boldsymbol{r}) = G(r)\left\{1 + \cos\left[2ks(1 - \delta k - \tfrac{1}{2}\beta^2) + \psi(\boldsymbol{r})\right]\right\}, \tag{3}$$

where

$$\psi(\boldsymbol{r}) = -c_1 r^2 - k/M\ \boldsymbol{r} \cdot (2\boldsymbol{\alpha} \times \hat{\boldsymbol{\zeta}}) + k/R\ \boldsymbol{r} \cdot \boldsymbol{d}, \tag{4}$$

and $M = (w/w_0)^2$ is a magnification factor which takes account of beam divergence. Details about calculations and approximations for obtaining Eq. (3) are given in [7]. In Eq. (3) the intensity profile

$$G(r) = \frac{2w_0^2}{w^2}\exp(-2r^2/w^2), \tag{5}$$

limits the interference pattern to $r \lesssim w$ and $\delta k = 2/(bkM)$ is a correction for the actual on-axis wavelength. The first term in Eq. (4), where

$$c_1 = \frac{4(w^2 - 2w_0^2)s}{bw^4} \approx \frac{ks}{R^2}, \quad w/w_0 \to \infty \tag{6}$$

originates from the curvature of the wave fronts and describes the interference pattern created by the superposition of nonconcentric spherical wave fronts which are tangent at $\boldsymbol{r} = 0$. The last terms originate from angular and position shearings and describe the interference pattern originated by the superposition of nonconcentric wave fronts which are tangent at $\boldsymbol{r} \neq \boldsymbol{0}$.

Additional insight into the phase of $I(\boldsymbol{r})$ can be gained by examining the interferometer operation by geometric optics. For the sake of simplicity, let us consider the interfering beams parallel, that is $\alpha = 0$, and the limit $w/w_0 \to \infty$, which corresponds to the spherical wave fronts having radius $R$. The ray hitting the observation plane at $\boldsymbol{r}$ undergoes the phase shift $2ks[1 - \gamma^2(\boldsymbol{r})/2]$. The projection angle is given by

$$\gamma(\boldsymbol{r}) = \frac{|\boldsymbol{r} - \boldsymbol{r}_m|}{R}, \tag{7}$$

$\boldsymbol{r}_m$ being the coordinate of the ray normal to the movable mirror and

$$\begin{aligned}\gamma^2(\boldsymbol{r}) &= \beta^2 + \frac{1}{R^2}r^2 - \frac{2\boldsymbol{r} \cdot \boldsymbol{r}_m}{R^2} \\ &= \beta^2 + \frac{1}{R^2}r^2 - \frac{2}{R}\boldsymbol{r} \cdot (\boldsymbol{\beta} \times \hat{\boldsymbol{\zeta}}),\end{aligned} \tag{8}$$

where $\beta = r_m/R$ is the projection angle of the beam axis. Consequently, apart from corrections required because of diffraction and nonparallelism, the phase of the interference pattern is given by the projection of the $2ks$ shift of the plane-wave wave front matching the interferometer movable mirror on the directions of all rays of the beam.

As a consequence of the overlapping of two spherical wave fronts having different curvatures, the interference pattern is formed by concentric circles, any two of them approaching each other with increasing distance from the common center. If diffraction is neglected, that is, if the first term is omitted in Eq. (4), and if $R \to \infty$, the interference pattern reduces to parallel fringes with spacing $\Lambda_\alpha = M\lambda/2\alpha$, as expected. Also the combined effect of diffraction and position shearing causes an interference pattern formed, in a first approximation, by a system of parallel fringe spacing. The relevant fringe spacing is $\Lambda_d = \lambda R/d$. It is worthwhile noting that it is impossible to distinguish angular and transverse shearings by merely looking at the interference pattern: in both cases the phase depends linearly on $\boldsymbol{r}$ and $I(\boldsymbol{r})$ resembles a system of parallel fringes. When the interference pattern is analyzed in order to evaluate the misalignment between the interfering wave fronts, transverse shearing leads to the measurement of a seeming rotation.

The exact calculation of the diffraction contribution to interferometric measurements requires that $I(\boldsymbol{r})$ be integrated over the relevant portions of the position-sensitive detector. For the sake of simplicity, rotations $\boldsymbol{\alpha}$ and $\boldsymbol{\beta}$ are assumed parallel and the detector is assumed centered on the beam axis and oriented at 45° to $\boldsymbol{\alpha} \times \hat{\boldsymbol{\zeta}}$ (which is the same direction as $\boldsymbol{\beta} \times \hat{\boldsymbol{\zeta}}$); then

$$\boldsymbol{r} \cdot (2\boldsymbol{\alpha} \times \hat{\boldsymbol{\zeta}}) = 2\alpha(x + y)/\sqrt{2}, \tag{9a}$$

$$\boldsymbol{r} \cdot \boldsymbol{d} = d(x + y)/\sqrt{2}, \tag{9b}$$

where the $x$ and $y$ axes have been taken along the borders of detector portions. The examination of a general configuration of the interferometer and the detector [13] does not further clarify the physics of the system, but merely complicates the mathematics. The overall power on each portion is given by the integral

$$S_i = \int_{A_i} I(x,y)\,dx\,dy = C + B\cos\left[2ks(1-\delta k-\beta^2/2)+\Psi_i\right], \tag{10}$$

which extends over the $i$th quadrant of the observation plane and in which

$$C = \int_{A_i} G(x,y)\,dx\,dy = \frac{\pi w^2}{8}, \tag{11a}$$

$$B^2 = \left\{\int_{A_i} G(x,y)\cos\left[\psi(x,y)\right]\,dx\,dy\right\}^2 + \left\{\int_{A_i} G(x,y)\sin\left[\psi(x,y)\right]\,dx\,dy\right\}^2 \tag{11b}$$

are independent (within the approximations here considered) of the specific quadrant over which the integration is carried out, and

$$\tan\Psi_i = \frac{\int_{A_i} G(x,y)\sin\left[\psi(x,y)\right]\,dx\,dy}{\int_{A_i} G(x,y)\cos\left[\psi(x,y)\right]\,dx\,dy}. \tag{11c}$$

Owing the presence of the function $G(r)$, if $\psi(r=w) \ll 1$, that is, in the case of a very small rotation, we can compute the integrals in Eq. (11c) by using the approximations $\cos\psi(x,y) \approx 1$, and

$$\sin\psi(x,y) \approx -c_1 r^2 - c_2(x+y)/\sqrt{2}, \tag{12}$$

where $c_2 = k(2\alpha/M - d/R)$, which gives $\Psi_i$ as the mean of $\psi(\boldsymbol{r})$ for each ray of the bundle weighted by the ray intensity $G(\boldsymbol{r})$. Then, by using [18]

$$\int_0^\infty t^2 e^{-at^2}\,dt = \frac{\sqrt{\pi a}}{4a^2}, \tag{13a}$$

and

$$\int_0^\infty t e^{-at^2}\,dt = \frac{1}{2a}, \tag{13b}$$

we obtain $\Gamma = 1$, $\Psi_{2,4} = -c_1 w^2/2$, and

$$\Psi_{1,3} = -\tfrac{1}{2}c_1 w^2 \mp \frac{w}{\sqrt{\pi}}c_2, \tag{14}$$

where $\Gamma = B/C$ is the contrast and the plus or minus sign refers to the first or third quadrant, respectively. In the case of a large rotation, a better approximation is obtained by setting $c_1 = 0$ in Eq. (4), an approximation allowed by the negligible value of the $c_1 r^2$ term with respect to the others. By using [18]

$$\int_0^\infty e^{-at^2}\cos(2xt)\,dt = \frac{1}{2}\sqrt{\frac{\pi}{a}}e^{-x^2/a} \tag{15a}$$

and

$$\int_0^\infty e^{-at^2}\sin(2xt)\,dt = \frac{1}{2}\sqrt{\frac{\pi}{a}}e^{-x^2/a}\mathrm{erfi}(x/\sqrt{a}), \tag{15b}$$

where $\mathrm{erfi}(z) = -i\,\mathrm{erfi}(z)$ is the imaginary error function, we obtain

$$\Gamma = \frac{1+\mathrm{erfi}(c_2 w/4)^2}{\exp\left[2(c_2 w/4)^2\right]}, \tag{16a}$$

$\Psi_{2,4} = 0$, and

$$\tan\Psi_{1,3} = \mp\frac{2\mathrm{erfi}(c_2 w/4)}{1-\mathrm{erfi}(c_2 w/4)^2}, \tag{16b}$$

where the plus or minus sign still refers to the first or third quadrant. The contrast and phase of the integrated signal and the range of application of the approximation (14) are shown in Fig. 4.

To simplify the analysis of the angle measurement principles, let us assume the interferometer perfectly aligned, $s = \alpha = 0$, and $\beta = 0$. The rotation $\alpha$ of the mirror causes the rotation $2\alpha$ of the measuring beam around the point $z_I$, the rotation $\beta = \alpha$ of the baseline, and the transverse shearing $d = -2\alpha z_I$. The mean phase shift between the top and bottom portions of the interference pattern is given by $\Delta\Psi = 2k\alpha D$, where

$$D = \frac{2w}{\sqrt{\pi}}\frac{R+Mz_I}{MR} \tag{17}$$

is the equivalent distance between the two spots. Two limits can be considered: the near field limit (plane wave) to which $M = 1$, $R = \infty$, and $D = 2w/\sqrt{\pi}$ will correspond, and the far field limit (spherical wave) to which $M = R = \infty$ and $D = 0$ will correspond. The null

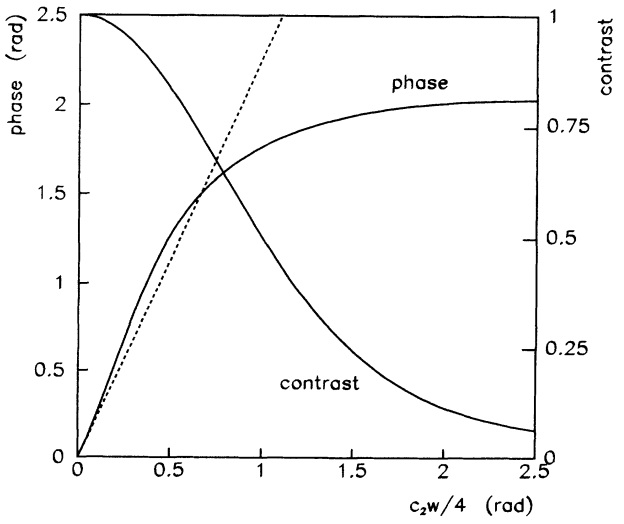


FIG. 4. Contrast and phase of fringes belonging to a single quadrant of the observation plane. The broken line is the lowest order approximation (14) of the phase.

spacing, which occurs also when $z_I = -R/M$, emphasizes the fact that the interference pattern is insensitive to rotation. In fact, in the foregoing cases, the rotation occurs at the curvature center of wave fronts (by using the relations given in [7,16] it can be proved that $z - z_I = z + R/M = R$) and, consequently, the interfering wave fronts are not shifted at all.

Equation (14) expresses formally the fact that diffraction and shearing jointly bring about a seeming rotation, which cannot be produced unless both phenomena are present at the same time. In fact, their contribution to phase combines with that of rotations through the ratio $d/R$ which is zero if $d = 0$ (no transverse shearing) or if $R \to \infty$ (no diffraction). As shown in Eq. (2) and in Fig. 1, mirror movement causes the interfering beams to shear laterally with respect to each other and this fact can be used to investigate experimentally the effect of shearing and diffraction. Let us consider the interfering beam collinear but the baseline imperfectly aligned so that, according to Eq. (2), transverse shearing, $d = 2s\beta$, varies linearly with mirror position. The mean phase shift between the top and bottom portions of the interference pattern is now given by $\Delta\Psi = 2k\alpha_d D$, where the seeming guiding error

$$\alpha_d = \frac{M\beta s}{R + Mz_I} \tag{18}$$

depends linearly on the mirror position and the baseline direction. This relation, which gives the error of the interferometric measurement of parasitic tilts accompanying the mirror movement in terms of the geometry of measurement, is central in the present work because it can be verified experimentally.

## IV. RESULTS

To assess the geometry of interference, the waist size and location were estimated from beam profile measurements at a sequence of points along the beam axis. Results are shown in Fig. 5, which gives also location of detector, $z = (1.6 \pm 0.2)$ m, and of interferometer, $z_I = (2.1 \pm 0.2)$ m. According to the convention adopted, the positive direction of the beam axis is toward the detector, so that, in the figure, the beam propagates from right to left, though measurements were actually carried out on the beam emerging from the interferometer. The spot size at the beam waist, $w_0 = (0.61 \pm 0.01)$ mm, and the confocal parameter, $b = (3.69 \pm 0.04)$ m, were obtained by fitting data by a hyperbola. The equivalent spacing between spots, $D = 1$ mm, calculated from these values by using Eq. (17), is in good agreement with the value obtained by the calibration of the angle interferometer [13].

When driving the interferometer to produce a uniform interference pattern we directly observe the beam astigmatism. By acting on mirror positions and tilts, a uniform interference pattern can be obtained only if the wave fronts are perfectly plane or spherical. In our specific case, the mean phase of the interference pattern is monitored at top (bottom) and left (right) portions, but only three degrees of freedom are available to match the interfering wave fronts, namely, a shift and two rotations. Consequently, since only three portions of the interference pattern can be driven to have the same mean phase, the excess of the fourth measures the astigmatism. The measured value is $\lambda/100$ over 1 mm offset.

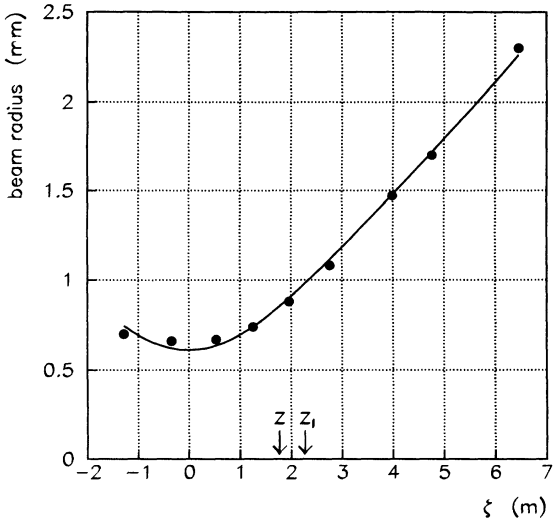


FIG. 5. Laser beam profile. The solid line is the best fit hyperbola and $z_I$ and $z$ are interferometer and detector locations.

The analyzer is guided orthogonally to the diffracting planes over displacements ranging from zero to one hundred micrometers and guiding errors (tilts) are compensated for by feeding the angle values into its adjusting elements. At both the start and end points, a few x-ray fringes are scanned. During scanning the photon counts relating to the top and bottom portions of the x-ray interference patterns and the corresponding top and bottom displacements of the analyzer are stored for subsequent

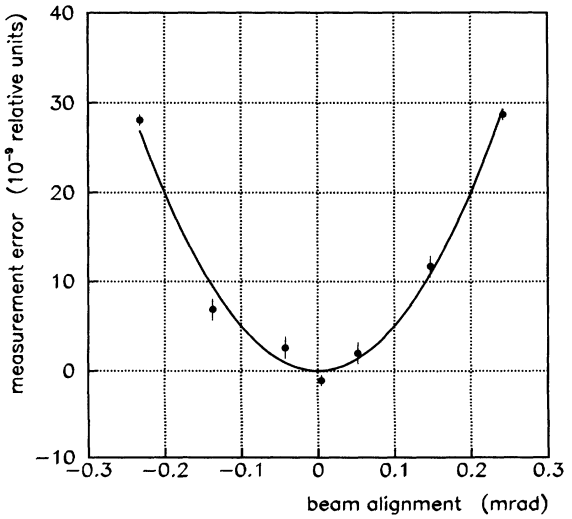


FIG. 6. Projection error of the optical interferometer in the measurement of 80 $\mu$m displacements vs laser beam alignment. The solid line is the best-fit parabola.

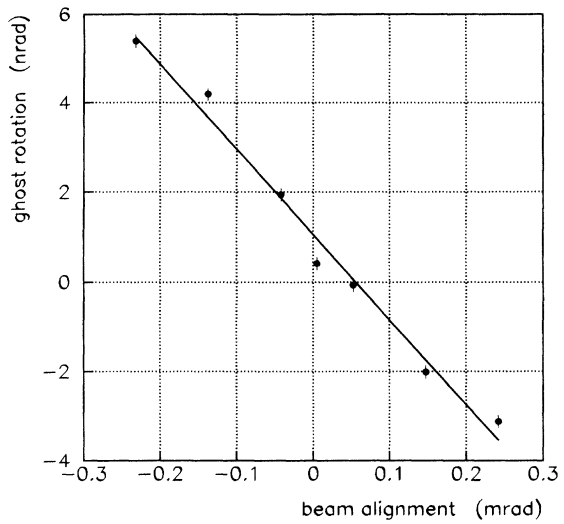


FIG. 7. Ghost rotation vs laser beam alignment. Analyzer displacement is $s = 80$ $\mu$m. The solid line is the best-fit straight line.

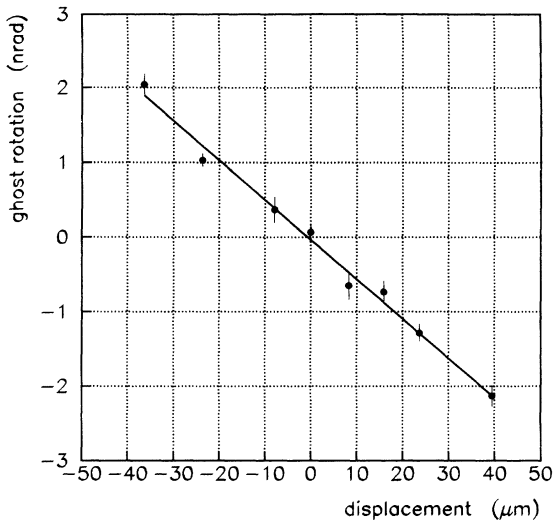


FIG. 8. Ghost rotation vs analyzer displacement. Alignment angle of the laser beam is $\beta = 0.24$ mrad. The solid line is the best-fit straight line.

analysis in order to compare the x-ray and optical measurement values of displacement and pitch.

To verify experimentally Eq. (18) the alignment angle $\beta$ of the laser beam is varied by tilting the optical fiber delivering the beam to the interferometer in the vertical plane. The projection error shown in Fig. 6 is given by the relative difference between the optical and the x-ray measurements of the analyzer displacement, that is, between displacement projections on the beam direction, which is varied by fiber tilting, and on the normal to the diffracting planes, which remain fixed. Unfortunately, in setting up the experiment, no device was mounted for on-line measurements of the incidence angle of the laser beam on the analyzer. Consequently, the voltage supplying the fiber tilter was put proportional to this angle. The angle origin and the scale factor were obtained by fitting the data in Fig. 6 according to the parabola $\beta^2/2$. The data shown in the figure refer to movements over 250 optical orders, about 80 $\mu$m, so that $10^{-8}$ relative errors correspond to $2.5\times10^{-6}$ relative errors in the subdivision of a single fringe. The figure exhibits clearly the very high sensitivity of combined x-ray and optical interferometry.

When the pitch is locked to the zero reading of the angle interferometer, the ghost rotation caused by the combined effects of diffraction and transverse shearing is corrected for by rotating the analyzer by a countersign angle. Since this rotation causes a phase shift between the top and bottom portions of the x-ray interference pattern, it can be easily measured [9]. Results are shown in Figs. 7 and 8. Solid lines are the fit of data according to the linear dependence on the baseline and on the analyzer position predicted by Eq. (18). The estimated slopes, $19.1\times10^{-6}$ and $5.3\times10^{-2}$ nrad/$\mu$m, agree with the values calculated by application of Eq. (18), namely, $18.7\times10^{-6}$ and $5.7\times10^{-2}$ nrad/$\mu$m.

Figure 7 shows also that the ghost rotation is not zero, as predicted by Eq. (18), when the projection error is minimum, that is, when $\beta = 0$. The nonzero value evidences wave front distortions other than astigmatism, which make curvature differ from one point to another in the beam cross section. In fact, if the geometric description (8) of the phase contributions to the interference pattern is recalled, it is evident that the absence of a constant term in Eq. (18) is a consequence of the assumption of a constant curvature.

## ACKNOWLEDGMENT

The authors are grateful for the support granted by the Commission of the European Communities under Contract No. 3422/1/0/182/91/4-BCR-D(30).

[1] W.J. Tango and R.Q. Twiss, Appl. Opt. **13**, 1814 (1974).
[2] K. Dorenwendt and G. Bonsch, Metrologia **12**, 57 (1976).
[3] J.-P. Monchalin, M.J. Kelly, J.E. Thomas, N.A. Kumit, A. Szoke, F. Zernike, P.H. Lee, and A. Javan, Appl. Opt. **20**, 736 (1981).
[4] G. Bonsch, Appl. Opt. **22**, 3414 (1983).
[5] G. Basile, A. Bergamin, G. Cavagnero, G. Mana, E. Vittone, and G. Zosi, IEEE Trans. Instrum. Meas. **40**, 98 (1991).
[6] G. Basile, A. Bergamin, G. Cavagnero, and G. Mana, Metrologia **28**, 455 (1992).
[7] G. Mana, Metrologia **26**, 87 (1989).
[8] U. Bonse and W. Graeff, in *X-ray Optics*, edited by H.-J. Quessier, Topics in Applied Physics Vol. 33 (Springer-Verlag, Berlin, 1977), pp. 93–143.
[9] A. Bergamin, G. Cavagnero, and G. Mana, Z. Phys. B **76**, 25 (1989).
[10] A. Bergamin, G. Cavagnero, and G. Mana, Meas. Sc.

Techn. **2**, 725 (1991).
[11] D. Windisch and P. Becker, J. Appl. Cryst. **25**, 377 (1992).
[12] G. Basile, A. Bergamin, G. Cavagnero, G. Mana, and G. Zosi, IEEE Trans. Instrum. Meas. **38**, 210 (1989).
[13] A. Bergamin, G. Cavagnero, and G. Mana, Rev. Sci. Instrum. **64**, 3076 (1993).
[14] A. Bergamin, G. Cavagnero, and G. Mana, J. Mod. Opt. **39**, 2053 (1992).
[15] A. Bergamin, G. Cavagnero, and G. Mana, Rev. Sci. Instrum. **64**, 168 (1993).
[16] H. Kogelnik and T. Li, Appl. Opt. **5**, 1550 (1966).
[17] J.W. Goodman, *Introduction to Fourier Optics* (McGraw-Hill, New York, 1968).
[18] *Handbook of Mathematical Functions,* edited by M. Abramowitz and I.A. Stegun (Dover, New York, 1964).

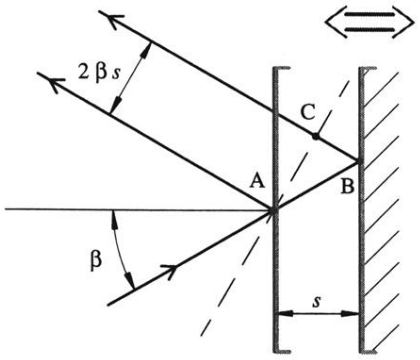


FIG. 1. Ray tracing of measuring beam reflection. The broken line represents a reflected wave front. From elementary geometry, longitudinal and transverse shearings are related to mirror displacement by $\overline{AB} + \overline{BC} = 2s(1 - \beta^2/2)$ and $\overline{AC} = 2\beta s$.

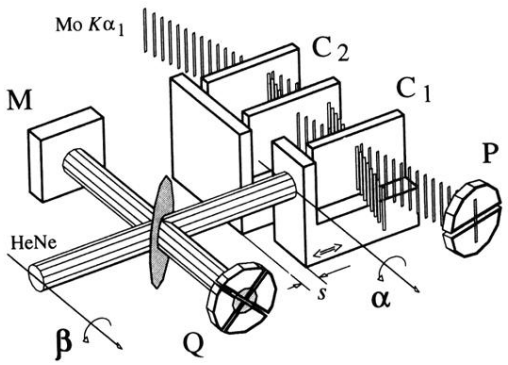


FIG. 2. Schematic drawing of the x-ray and optical interferometer. Mo $K\alpha_1$ x-ray beam, C1 and C2 fixed and movable (analyzer) crystals of the x-ray interferometer, P and Q position-sensitive detectors, He-Ne laser beam, M fixed mirror. X-ray and optical fringes are scanned by moving the analyzer over the distance $s$. Laser beam and interferometer alignments are varied by tilting the beam-delivering fiber (rotation $\boldsymbol{\beta}$) and the analyzer (rotation $\boldsymbol{\alpha}$).